Modular transient nanoclustering of activated β2-adrenergic receptors revealed by single-molecule tracking of conformation-specific nanobodies

Rachel S. Gormal[a], Pranesh Padmanabhan[a], Ravikiran Kasula[a,1], Adekunle T. Bademosi[a,1], Sean Coakley[a], Jean Giacomotto[b,c], Ailisa Blum[a], Merja Joensuu[a,d], Tristan P. Wallis[a], Harriet P. Lo[e], Srikanth Budnar[e], James Rae[e], Charles Ferguson[e], Michele Bastiani[e], Walter G. Thomas[f], Els Pardon[g,h], Jan Steyaert[g,h], Alpha S. Yap[e], Geoffrey J. Goodhill[b,i], Massimo A. Hilliard[a], Robert G. Parton[e,j], and Frédéric A. Meunier[a,2]

[a]Clem Jones Centre for Ageing Dementia Research, Queensland Brain Institute, The University of Queensland, Brisbane, QLD 4072, Australia; [b]Queensland Brain Institute, The University of Queensland, Brisbane, QLD 4072, Australia; [c]Queensland Centre for Mental Health Research, West Moreton Hospital and Health Service and University of Queensland, Brisbane, QLD 4072, Australia; [d]Minerva Foundation Institute for Medical Research, 00290 Helsinki, Finland; [e]Institute for Molecular Bioscience, The University of Queensland, Brisbane, QLD 4072, Australia; [f]School of Biomedical Sciences, The University of Queensland, Brisbane, QLD 4072, Australia; [g]Structural Biology Brussels, Vrije Universiteit Brussel, 1050 Brussels, Belgium; [h]VIB-VUB Center for Structural Biology, VIB, 1050 Brussels, Belgium; [i]School of Mathematics and Physics, The University of Queensland, Brisbane, QLD 4072, Australia; and [j]Centre for Microscopy and Microanalysis, The University of Queensland, Brisbane, QLD 4072, Australia

Edited by Satyajit Mayor, National Centre for Biological Sciences, Bangalore, India, and approved August 12, 2020 (received for review April 23, 2020)

None of the current superresolution microscopy techniques can reliably image the changes in endogenous protein nanoclustering dynamics associated with specific conformations in live cells. Single-domain nanobodies have been invaluable tools to isolate defined conformational states of proteins, and we reasoned that expressing these nanobodies coupled to single-molecule imaging-amenable tags could allow superresolution analysis of endogenous proteins in discrete conformational states. Here, we used anti-GFP nanobodies tagged with photoconvertible mEos expressed as intrabodies, as a proof-of-concept to perform single-particle tracking on a range of GFP proteins expressed in live cells, neurons, and small organisms. We next expressed highly specialized nanobodies that target conformation-specific endogenous β_2-adrenoreceptor (β_2-AR) in neurosecretory cells, unveiling real-time mobility behaviors of activated and inactivated endogenous conformers during agonist treatment in living cells. We showed that activated β_2-*AR* (Nb80) is highly immobile and organized in nanoclusters. The Gαs–GPCR complex detected with Nb37 displayed higher mobility with surprisingly similar nanoclustering dynamics to that of Nb80. Activated conformers are highly sensitive to dynamin inhibition, suggesting selective targeting for endocytosis. Inactivated β_2-*AR* (Nb60) molecules are also largely immobile but relatively less sensitive to endocytic blockade. Expression of single-domain nanobodies therefore provides a unique opportunity to capture highly transient changes in the dynamic nanoscale organization of endogenous proteins.

single-particle–tracking superresolution microscopy | nanobodies | β2-adrenoreceptor

Superresolution microscopy, in particular single-molecule localization techniques, such as stochastic optical reconstruction microscopy and photoactivated localization microscopy (PALM), are widely employed research tools (1–5) that are advancing our understanding of the nanoscale organization of biological structures and processes. These techniques rely on a similar principle that limited subsets of spatially resolvable fluorophores are activated at any one time, so that their precise position can be determined within the diffraction-limited spot of each emitter. Through iterations of this process, the precise spatial organization of proteins can be determined. Furthermore, the mobility states of single proteins can be monitored in living cells by single-particle–tracking PALM (sptPALM), which generates spatially resolved maps of single-molecule trajectories (4, 6, 7).

Both PALM and sptPALM require overexpression of proteins of interest tagged with photoactivatable/photoconvertible labels. Overexpression has its disadvantages and requires careful controls to avoid obvious pitfalls (e.g., potential mislocalization and aggregation) (8, 9). Morever, because only a small minority of proteins are active at any one time, overexpression is not suited to tracking changes in mobility and clustering associated with specific activity-dependent conformational changes. This limits our understanding of the dynamic nanoscale organization associated with proteins performing their functions.

Single-domain antibodies, also known as nanobodies, are small (15 kDa) antigen-binding fragments produced in camelids (10). Owing to their small size and ease of expression in various systems, they are invaluable tools to localize, purify, and crystalize defined conformational states of proteins of interest (11). Nanobodies have been developed to bind GFP with high affinity (12, 13). Anti-GFP nanobodies, also referred to as GFP-binding proteins (GBPs), are ideal for superresolution microscopy of GFP-labeled proteins, as they are small, highly soluble single-domain

Significance

Proteins moving freely on the plasma membrane can become transiently trapped in functionally essential clusters. This capability is likely to be influenced by subtle conformational states of the protein promoting or preventing such confinement. The downside of conventional imaging of overexpressed tagged proteins is that it precludes selective tracking of inherently minor albeit functionally essential conformer populations. Intracellular expression of single-chain nanobodies allowed us to track endogenous proteins in highly specific conformational states in live cells and small organisms. We unveiled the full scope of nanoclustering behavior of β_2-adrenergic receptors in various conformations, along with their transient nature. This technique is broadly applicable to other proteins and will help unravel essential dynamics and organization of nanoclusters.

Author contributions: R.S.G., S.C., J.G., and F.A.M. designed research; R.S.G., R.K., A.T.B., S.C., J.G., A.B., M.J., S.B., J.R., C.F., and M.B. performed research; R.S.G., M.J., H.P.L., W.G.T., E.P., J.S., A.S.Y., G.J.G., M.A.H., and R.G.P. contributed new reagents/analytic tools; R.S.G., P.P., R.K., A.T.B., A.B., M.J., T.P.W., J.R., and C.F. analyzed data; and R.S.G., P.P., R.K., A.T.B., and F.A.M. wrote the paper.

The authors declare no competing interest.

This article is a PNAS Direct Submission.

[1]R.K. and A.T.B. contributed equally to this work.

[2]To whom correspondence may be addressed. Email: f.meunier@uq.edu.au.

This article contains supporting information online at https://www.pnas.org/lookup/suppl/doi:10.1073/pnas.2007443117/-/DCSupplemental.

First published November 19, 2020.

antibody fragments that can be tagged with bright fluorescent organic dyes (14). Purified GBPs have already been used in single-molecule imaging, namely, universal Point Accumulation for Imaging in Nanoscale Topography (uPAINT) as well as for immunocytochemical staining on fixed cells (15). One current uPAINT application involves the use of a GBP tagged with an organic dye (e.g., Atto) to track extracellular GFP-labeled receptors in cultured cells and in dual-color systems (16). However, uPAINT is limited to tracking receptors with extracellular epitopes (17, 18). More recently, a similarly labeled GBP has been used in a pulse–chase strategy to track endocytic structures in neurons, such as recycling synaptic vesicles by single-molecule imaging using a technique known as subdiffractional Tracking of Internalized Molecules (19). This approach has also been used to study axonal retrograde transport following internalization (20, 21). However, cytoplasmic-facing epitopes remain inaccessible by either approach.

Immunoglobulin antibodies expressed in cells as "intrabodies" have also been previously used in cell biology. However, their large size (150 kDa) and their propensity to aggregate within the reducing environment of the cytosol have limited their application in cells. Consequently, smaller modified formats such as single-chain (ScFv, Fab)/single-domain antibodies (nanobodies) are increasingly becoming the standard, as they are significantly smaller (10 kDa to 15 kDa), are composed of a monomeric variable antibody domain, retain their antigen-binding affinity (22), and are more resistant to the reducing environment of the cytosol when expressed in living cells as intrabodies (23–25). Indeed, nanobodies have been effectively expressed as intrabodies to block viral production (26) as well as clostridial neurotoxin activity (27). Therefore, we reasoned that intracellularly expressed nanobodies could potentially be used as intrabodies to perform single-molecule imaging of endogenous proteins located on the plasma membrane with intracellular epitopes.

Here, we report the use of nanobodies expressed as intrabodies through a technique we have called Fluorescent intrabody Localization Microscopy (FiLM). We first generated a proof-of-concept of the technique by coexpressing anti-GFP nanobodies, tagged with the photoconvertible fluorescent protein mEos2, along with the pleckstrin homology domain of phospholipase C delta (PH-PLCδ) fused with GFP (28). This allowed us to image plasma membrane domains enriched in phosphoinositide PtdIns(4,5)P_2 by total internal reflection fluorescence (TIRF) microscopy in living neurosecretory PC12 cells. Using FiLM, we achieved single-molecule imaging with mobilities indistinguishable from control PH-PLCδ directly tagged with mEos2, using sptPALM (4). We further demonstrated that FiLM can be used on a range of other protein targets, including the enzyme phosphatidic acid preferring phospholipase A1 (PA-PLA1), an adhesion junction protein (E-cadherin), a structural protein (caveolin), and a fusogen (EFF-1), in primary cultured neurons and epithelial cells, as well as in small organisms *Danio rerio* (zebrafish) and *Caenorhabditis elegans*. Finally, we applied FiLM to track conformation-specific nanobodies selectively binding endogenous β_2-adrenergic receptors (β_2-ARs). These nanobodies selectively recognize activated β_2-ARs (Nb80) (29, 30), the Gαs protein, when coupled to gene protein-coupled receptors (GPCRs) (Nb37) (29, 31) and inactivated β_2-ARs (Nb60) (32). Imaging these conformational-specific nanobodies on endogenous β_2-AR in neurosecretory PC12 cells revealed distinct dynamics and effects during agonist treatment when compared to the overexpressed β_2-AR. The activated form of the β_2-ARs had lower mobility (Nb80) when compared to Nb37. Using these conformational-specific nanobodies, we were able to detect a highly specific effect upon endocytic blockade on the activated receptors, suggesting specificity in internalization of activated species. In addition, we found that these nanoclusters postulated to represent signaling nanoplatforms are transient and entwined with the endocytic process.

Results

Intrabodies to Detect Intracellular Proteins at the Plasma Membrane. We first investigated whether an anti-GFP nanobody known as GBP could be expressed as an intrabody in cells to correctly localize GFP-tagged proteins. To test this approach, we coexpressed the PtdIns(4,5)P_2 binding probe, PH-PLCδ tagged with EGFP (PH-PLCδ^{WT}-EGFP) (*SI Appendix*, Fig. S1*A*) and GBP-mCherry (*SI Appendix*, Fig. S1*B*) in PC12 cells, the expectation being that GBP-mCherry would bind to its GFP target and therefore colocalize with PH-PLCδ^{WT}-EGFP (*SI Appendix*, Fig. S1*C*). The cells were then fixed, and imaged using confocal microscopy. PH-PLCδ^{WT}-EGFP exhibited plasma membrane localization due to its binding to PtdIns(4,5)P_2, as previously described (28). As expected, GBP-mCherry colocalized with PH-PLCδ^{WT}-EGFP at the plasma membrane (*SI Appendix*, Fig. S1 *D*, *Top*). Control experiments were carried out by cotransfecting PC12 cells with GBP-mCherry and a PtdIns(4,5)P_2 binding-deficient mutant (PH-PLCδ^{R40L}-EGFP) which mislocalizes to the cytosol (28) (*SI Appendix*, Fig. S1 *D* and *E*). In this case, the GBP-mCherry signal was also cytosolic, demonstrating that the GBP nanobody can be used as a proxy to correctly mimic the expression pattern of GFP-tagged proteins of interest. We also performed three-dimensional electron tomography to determine whether the GBP localized to the plasma membrane in our cellular system using the APEX labeling approach (33). This analysis revealed that GBP-APEX was indeed correctly targeted to the plasma membrane upon coexpression of PH-PLCδ^{WT}-EGFP in PC12 cells (Movie S1 and *SI Appendix*, Fig. S2).

From sptPALM to FiLM: Single-Molecule Tracking of GBP-mEos2 in PC12 Cells. Having demonstrated that GBP can be used to localize GFP-tagged proteins in PC12 cells, we next tested whether it was amenable to single-molecule localization and tracking using superresolution microscopy. By generating GBP tagged with a photoconvertible fluorescent protein, we aimed to establish whether it would allow single-particle tracking of PH-PLCδ^{WT}-EGFP, which is known to be organized in nanoclusters (34)—a technique we call FiLM (Fig. 1 *A* and *B*). We first generated PH-PLCδ^{WT} tagged with the photoconvertible protein mEos2 (PH-PLCδ^{WT}-mEos2) in order to perform classical sptPALM, which allows the nanoscale localization and tracking of individually expressed proteins (4). Individual molecules of PH-PLCδ^{WT}-mEos2 were imaged by stochastically photoconverting mEos2 from green to red emission using low 405-nm laser power with TIRF microscopy. We first captured a low-resolution TIRF image of the PH-PLCδ^{WT}-mEos2 on the plasma membrane prior to photoconversion in the green emission channel (Fig. 1*C*). We then performed sptPALM, and acquired a time series of molecular detections (50 Hz) in the red emission channel during PH-PLCδ^{WT}-mEos2 photoconversion, as previously described (4). The movie was analyzed using the PALMtracer software to track single molecules (35). A region of interest from a representative cell is illustrated in Fig. 1*C*, together with the superresolved maps of the intensities (Fig. 1*D*), the diffusion coefficients (Fig. 1*E*), and the single-molecule trajectories (Fig. 1*F*) obtained from this region. The equivalent data were also produced using the FiLM technique, from cells coexpressing PH-PLCδ^{WT}-EGFP and GBP-mEos2 (Fig. 1 *G*–*J*). Nanodomains of PH-PLCδ^{WT} were detected with both sptPALM and FiLM (see intensity maps in Fig. 1 *D* and *H*), and were easily identified in the spatial maps of diffusion coefficients (Fig. 1 *E* and *I*), with highly confined trajectories being detected within these nanodomains (Fig. 1 *F* and *J*). We then compared the mobility of PH-PLCδ^{WT}-mEos2 (by sptPALM) to that of GBP-mEos2 in PC12 cells coexpressing PH-PLCδ^{WT}-EGFP (by FiLM; Fig. 1 *K*–*N* and Movies S2 and S3). We calculated the average mean square

CELL BIOLOGY

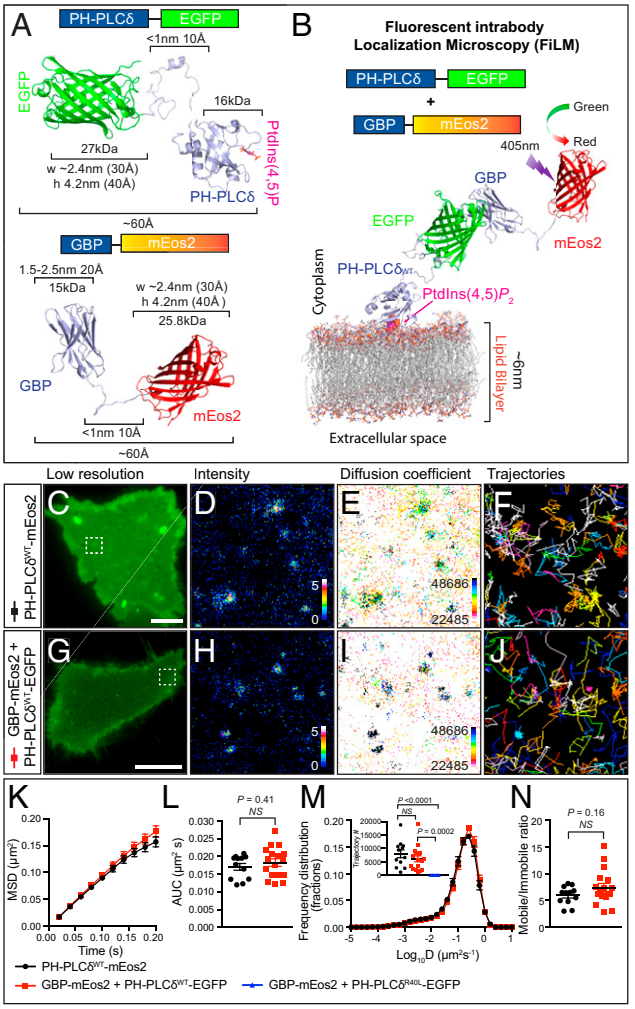

Fig. 1. Single-particle detection of PH-PLCδ^{WT}-EGFP by GBP-Nb-mEos2 using the FiLM technique. (*A*) Expression of PH-PLCδ^{WT}-EGFP (GFP target) (*Top*) together with GBP-mEos2 (*Bottom*) facilitates single-particle tracking in cellular transfection systems. (*B*) Illustration of the principle of FiLM using PH-PLCδ^{WT}-EGFP target at the plasma membrane. (*C*) A representative PC12 cell in TIRF shows the green fluorescence of PH-PLCδ^{WT}-mEos2 prior to photoconversion. (Scale bar, 5 μm.) (The region of interest, defined by the white box, is used for *D*–*F*.) Superresolution imaging was performed at 50 Hz with analysis of movies generating (*D*) sptPALM average intensity map, (*E*) diffusion coefficient distribution (darker colors represent lower mobility), and (*F*) trajectory map (color coded by time; warmer colors acquired later into the acquisition). (*G*) PC12 cell expressing PH-PLCδ^{WT}-EGFP and GBP-mEos2 (*H*–*J* as per *D*–*F*). (Scale bar, 5 μm.) (*K*) Analysis of single-particle tracking was expressed as the MSD as a function of time, (*L*) AUC, (*M*) frequency distribution of the diffusion coefficient (*Inset*: trajectory number), and (*N*) mobile-to-immobile ratio (n = 12 and 17, cells for each condition from three independent experiments, PH-PLCδ^{R40L}-EGFP n = 10). Protein structures were generated in PyMOL. Statistics of AUC and mobile-to-immobile ratio were performed using an unpaired Student's t test. The differences between the two conditions were all nonsignificant (NS). Nonparametric ANOVA Kruskal–Wallis test with Dunn's multiple comparisons test was used to compare trajectory numbers between the three conditions.

displacement (MSD) over time (Fig. 1*K*) as well as the area under the MSD curve (AUC) (Fig. 1*L*). We also quantified the diffusion coefficient of individually tracked molecules and plotted the frequency distribution of the Log_{10} of the diffusion coefficient (Fig. 1*M*), expressing it as a ratio of the mobile to immobile populations (Fig. 1*N*), as previously described (6, 7, 19, 21). In all of these tests, we found that the results obtained using PH-PLCδ^{WT}-mEos2 (by sptPALM) and GBP-mEos2 in cells coexpressing PH-PLCδ^{WT}-EGFP (by FiLM) were statistically indistinguishable (Fig. 1 *K*–*N*). To test the reliability of our tracking system and selectivity of the GBP-mEos2, we coexpressed PtdIns(4,5)P2-binding deficient mutant PH-PLCδ^{R40L}-GFP. As expected with such a cytosolic probe, we found almost no tracks by using the GBP-mEos2 when we coexpressed it with PH-PLCδ^{R40L}-GFP (Fig. 1 *M*, *Inset*). In addition, we tracked a destabilized variant GBP tagged with mEos2 coexpressed with PH-PLCδ^{WT}-GFP. This destabilized GBP was previously shown to reduce the free cytosolic pool of the intrabody via degradation of unbound GBP (36, 37). The results obtained were indistinguishable from those achieved with GBP-mEos2, demonstrating that our tracking technique captures the GBP-mEos2 molecules bound to their target proteins (*SI Appendix*, Fig. S3).

We next compared sptPALM and FiLM by expressing PA-PLA1 (38) tagged with mEos2 (mEos2-PA-PLA1) or GFP-PA-PLA1 together with GBP-mEos2 in cultured rat hippocampal neurons. Low- and high-resolution images revealed the presence of PLA1 in neurites and its accumulation in synaptic regions with both techniques (*SI Appendix*, Fig. S4). Again, the mobility of PA-PLA1 as observed via sptPALM or FiLM was identical (*SI Appendix*, Fig. S4). We also successfully used the FiLM technique to image E-cadherin-GFP at the nanoscale level in adhesion junctions in cultured monolayers of Caco2 cells genetically engineered to express endogenous levels of GFP-tagged E-cadherin (*SI Appendix*, Fig. S5).

Together, these results indicate that the expression of GBP-mEos2 as a proxy to target GFP-tagged proteins is a valid alternative to expressing mEos2-tagged proteins, as both approaches generated statistically indistinguishable quantitative data of single-molecule mobility using sptPALM in live neurosecretory PC12 cells and hippocampal neurons.

In Vivo FiLM: Single-Molecule Tracking of GFP-Tagged Proteins Using GBP-mEos2 in Living Zebrafish *and C. elegans*. Although a wide variety of transgenic animals expressing GFP-tagged wild-type or mutant proteins is available, these lines are not easily amenable to superresolution microscopy (4, 6, 7, 17). We therefore tested whether FiLM could be used to bypass the need to generate new libraries of transgenic animals with appropriate photoconvertible tags. We first tested FiLM in *D. rerio* (zebrafish) in vivo. Caveolins 1 to 3 (Cav1 to Cav3) are membrane-bound scaffolding proteins that are essential components of caveolae, with Cav1 and Cav3 being required for their formation in nonmuscle and muscle cells, respectively (39, 40). We used a Cav3-GFP transgenic zebrafish strain to test whether we could perform superresolution FiLM by simply coexpressing the GBP-mEos2 in these animals. An RNA encoding GBP-mEos2 was synthesized and injected into one- to four-cell stage embryos. At 48 h to 72 h postfertilization (hpf), the fish were anesthetized and mounted for FiLM imaging (Fig. 2*A*). A low-resolution image of Cav3-GFP expression was acquired in the superficial dorsal muscle fiber layer (Fig. 2*B*) using oblique illumination (6, 41) to optimize the visualization of the muscle fibers. We then performed FiLM imaging of the GBP-mEos2 coexpressed in these muscle fibers (Movie S4) and tracked single molecules, generating super-resolved maps of intensities (Fig. 2 *C* and *D*), diffusion coefficients (Fig. 2*E*), and trajectories (Fig. 2 *F* and *G*). Nanodomains reminiscent of caveolae could be detected in vivo, with nanoclusters containing highly confined molecules (Fig. 2*G*). Although Cav3 is muscle specific, nonmuscle cells require Cav1 expression to form caveolae (42, 43). By way of comparison, we therefore expressed mEos2-Cav1 in Madin–Darby canine kidney (MDCK) cells to perform sptPALM (Fig. 2 *H*–*K*), revealing nanodomains of highly confined Cav1 molecules (Fig. 2*K*). We also compared the mobility of Cav3 and Cav1, in living muscle fibers and MDCK cells, respectively. Although there was a subtle difference between the

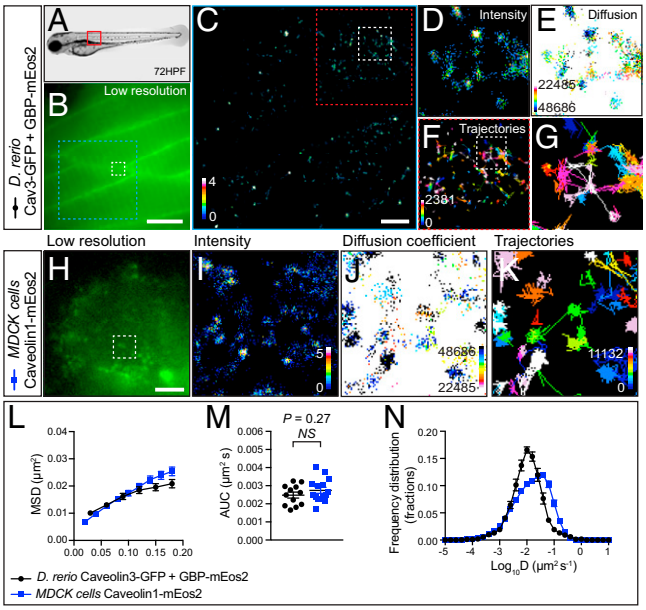

Fig. 2. Single-particle detection of Cav3-GFP in zebrafish by GBP-mEos2 using the FiLM technique. (*A*) Representative image of a 72-hpf zebrafish embryo. (*B*) Low-resolution image of the green fluorescence observed within skeletal muscle fibers of a zebrafish expressing Cav3-GFP as well as GBP-mEos2 at the location indicated by the red box in *A*. (Scale bar, 10μm). Superresolution imaging was performed at 33 Hz with analysis of movies generating (*C* and *D*) an average intensity map, (*E*) a diffusion coefficient map (darker colors represent lower mobility), and (*F*) a trajectory map (color coded by time; warmer colors acquired later into the acquisition). (Scale bar, *C*, 2.5 μm). (*G*) Illustrates the dual confinement trajectories within the region of interest in *F*. Red box (8 μm × 8 μm). (*H*) Low-resolution image of mEos2-Cav1 in transfected MDCK cells prior to photoconversion with a 405-nm laser. The region of interest is indicated with a white box (2 μm × 2 μm) in *H*. Superresolution imaging was performed at 50 Hz and analysis of movies generated (*I*) average intensity map, (*J*) diffusion coefficient map, and (*K*) trajectory map. Analysis of single-particle tracking was expressed as the (*L*) MSD as a function of time; (*M*) AUC, and (*N*) frequency distribution of the diffusion coefficient ($n = 12$ zebrafish from three independent injections; $n = 15$ MDCK cells from three independent experiments). Statistics of AUC were performed using an unpaired Student's *t* test.

MSDs, the AUC revealed no significant difference, suggesting that Cav1 and Cav3 may exhibit similar diffusion patterns in each system (Fig. 2 *L* and *M*). However, there was a slight difference between the frequencies of diffusion coefficients in the two systems, possibly reflecting the differences between caveolin in cultured cells and muscle fibers (Fig. 2*N*).

We next tested FiLM in the nematode *C. elegans* as an alternative in vivo model. EFF-1 is a fusogen that mediates a wide range of developmental cell fusion events in *C. elegans* (44, 45), as well as dendrite remodeling (46, 47) and a particular type of axonal repair known as axonal fusion (48, 49). We first generated transgenic strains expressing EFF-1::mEos2 under the promoter of the gene *mec-4* (*Pmec-4*), which drives expression specifically in mechanosensory neurons, and imaged the PLM mechanosensory neuron in the tail of the animal (Fig. 3 *A* and *B*). The animals were mounted on agarose pads and anesthetized for single-particle tracking. Low-resolution images of EFF-1::mEos2 expression were acquired in the PLM mechanosensory neuron in a region centered on the cell soma (Fig. 3*C*) using oblique illumination to optimize visualization. We then generated superresolved images, including trajectory maps (Fig. 3*D*), intensity (Fig. 3*E*), and diffusion coefficient (Fig. 3*F*). For comparative purposes, we also created additional lines which expressed both EFF-1::GFP and GBP::mEos2 under the same *Pmec-4* promoter and performed FiLM imaging and tracking of GBP-mEos2 within the PLM mechanosensory neuron (Fig. 3 *G–J* and Movies S5 and S6). We then carried out statistical analysis comparing the mobility patterns of EFF-1::mEos2 (sptPALM) and EFF-1::GFP plus GBP:mEos2 (FiLM) in living animals. This revealed that, although there was a subtle difference in the MSDs and the distribution of diffusion coefficients, the average values were indistinguishable (Fig. 3 *K–N*). Our data provide a proof of principle that anti-GFP nanobody expressed as intrabody can serve as a proxy for GFP-tagged protein, allowing their localization and tracking at a nanoscale level.

Single-molecule imaging of G-protein–coupled β_2-ARs in neurosecretory PC12 cells. Expression of single-domain nanobodies provides a unique opportunity to capture any highly transient changes in the nanoscale organization of signaling platforms. GPCR-mediated cell signaling tightly regulates a wide range of biological processes, including neurotransmission, cellular differentiation, and the immune response (50). One of the prototypical members of the GPCR family is the β_2-AR, which interacts with its cognate G protein (Gαs) to trigger downstream signaling. Using superresolution imaging techniques, it was recently found that the interaction between the β_2-AR and Gαs, and the subsequent activation of Gαs, occur in specific nanodomains or hot spots at the plasma membrane, suggesting a functional role of these nanodomains in GPCR signaling (51, 52). However, whether the single-molecule dynamics and nanoclustering are dependent on conformational states of GPCRs is currently unknown. Furthermore, it is yet to be determined whether these form transient or long-lived nanoclusters. We performed FiLM experiments to address these questions.

Isoprenaline-dependent immobilization of β_2-ARs in neurosecretory PC12 cells. We first expressed β_2-AR-YFP and GBP-mEos2 in PC12 cells and performed single-particle tracking before and after activation of β_2-ARs by isoprenaline (10 μM). YFP and GFP are conserved in all residues involved in the GFP–nanobody interface, so they both bind to GBP (12, 13). A representative cell is shown in Fig. 4*A*, and a region of interest from this cell is illustrated in Fig. 4 *B–G*. We then compared the mobility of β_2-AR-YFP by FiLM before and after agonist treatment (Fig. 4 *H–K*). The MSD, AUC, and the mobile to immobile ratio decreased in response to isoprenaline (Fig. 4 *H–K*). The diffusion coefficient distribution shifted to the left, indicating that the mobility of β_2-AR-YFP significantly decreased (Fig. 4 *J* and *K*). To further dissect the effect of isoprenaline on the mobility of β_2-AR-YFP, we analyzed the β_2-AR-YFP trajectories using hidden Markov models (HMM; see *Materials and Methods*). This analysis estimates the hidden diffusive states and associated state parameters from sets of experimentally measured trajectories (6, 19, 53). β_2-AR-YFP molecules switched between at least three distinct diffusive states, immobile (S1), intermediate (S2), and fast (S3) states (Fig. 4 *L* and *M*). Interestingly, the state occupancy of β_2-AR-YFP molecules in the immobile and intermediate states significantly increased following isoprenaline treatment, whereas the occupancy in the fast state decreased significantly (Fig. 4 *L* and *M*). Molecules that are in the immobile state with very low diffusion are generally thought to form nanoclusters (54, 55), suggesting that β_2-AR-YFP molecules are organized in distinct membrane nanodomains. Indeed, clusters of mGluR3, a member of the GPCR family, have been associated with the immobile state (55). Our data show that isoprenaline increases the S1 (immobile) state occupancy, indicating further nanoclustering of β_2-AR-YFP following agonist treatment in PC12 cells (Fig. 4*M*).

Inhibiting dynamin-dependent endocytosis reduces the mobility of β_2-AR-YFP. β_2-AR has recently been shown to be internalized in response to agonist-induced activation in early endosomes, where it contributes to a second phase of intracellular signaling (29). Further, β_2-AR has been previously demonstrated to undergo dynamin-dependent endocytosis (56). We next investigated whether the observed activity-dependent decrease in β_2-AR mobility is contingent on endocytosis. We took advantage of the

CELL BIOLOGY

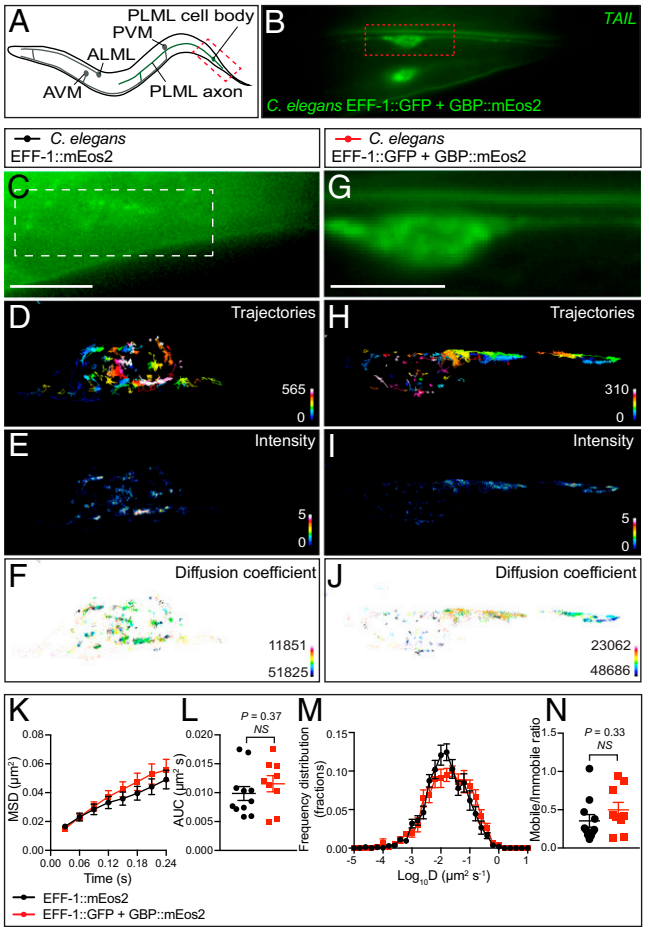

Fig. 3. Single-particle detection of EFF-1::GFP in *C. elegans* by GBP-mEos2 using the FiLM technique. (*A*) Illustration showing the location of the mechanosensory neurons in *C. elegans* driven by *Pmec-4* promoter expression. The portion of the PLM mechanosensory neuron imaged in these experiments is delineated by a red box. (*B*) Low-resolution image of the tail of a representative animal showing both left and right PLM mechanosensory neurons expressing *Pmec-4::eff-1::gfp* and *Pmec-4::mEos2-N1-GBP-Nb*. (*C*) Representative *C. elegans* PLM mechanosensory neuron in TIRF, expressing *Pmec-4::eff-1::Eos2* taken prior to photoconversion with a 405-nm laser. (Scale bar, 5 μm.) Region of interest defined by the white box is used for *D–F*. Superresolution imaging was performed at 33 Hz and analysis of the movies generated (*D*) a trajectory map (color coded by time; warmer colors acquired later into the acquisition), (*E*) an average intensity map, and (*F*) a diffusion coefficient map (darker colors represent lower mobility). (*G*) *C. elegans* expressing *Pmec-4::eff-1::gfp* and *Pmec-4::mEos2-N1-GBP-Nb* (Scale bar as in *C*) (*H–J* as per *D–F*). Analysis of single-particle tracking was expressed as the (*K*) MSD as a function of time, (*L*) AUC, (*M*) frequency distribution of the diffusion coefficient, and (*N*) mobile to immobile ratio ($n = 11$ and 9, animals for each condition from three independent experiments). Statistics of AUC were performed using an unpaired Student's *t* test, and a nonparametric Mann–Whitney *U* test was used to compare the mobile-to-immobile ratios.

dynamin inhibitor, Dyngo4a (57–59), to determine the contribution of endocytosis on the immobilization of the receptor. We expressed β_2-AR-YFP and GBP-mEos2 in PC12 cells in the presence of Dyngo4a (30 μM) or vehicle (dimethyl sulfoxide [DMSO]). Cells were imaged before and after treatment with isoprenaline (10 μM). As above (Fig. 4), isoprenaline decreased the mobility of β_2-AR-YFP in DMSO-treated cells (Fig. 5 *A* and *B*). Dyngo4a alone visibly decreased the mobility of β_2-AR-YFP in unstimulated cells, suggesting that blocking endocytosis has a general effect on the mobility of β_2-AR-YFP regardless of stimulation (Fig. 5 *A–D*). However, isoprenaline-dependent immobilization of β_2-AR-YFP occurred even in the presence of dynamin inhibitor, which was confirmed quantitatively with the analysis of the MSD and the frequency distribution of the diffusion coefficients (Fig. 5 *E–H*). These results demonstrate that the isoprenaline-mediated decrease in β_2-AR-YFP mobility is independent of endocytosis, suggesting two concurrent modes of clustering.

Conformational specific nanobodies reveal highly distinct mobility patterns of active and inactive β_2-AR conformers. β_2-AR is in a state of dynamic equilibrium and undergoes conformational state changes that underpin activation, G-protein coupling, and inactivation/desensitization (60). These biologically relevant conformations have been characterized with selective single-domain nanobodies that exclusively recognize these defined states (30, 61). Having shown proof-of-concept that nanobodies can be used to perform single-molecule imaging of GFP-tagged proteins, we reasoned that they could allow selective imaging of endogenous β_2-AR in these functionally relevant conformations and could therefore provide critical additional insights on their nanoscale organization. We generated mEos2-tagged Nb80, which recognizes the activated conformation of the β_2-AR, Nb37-mEos2, which selectively binds the guanine nucleotide-free form of Gαs- protein GPCRs, and Nb60-mEos2, which recognizes one of the inactive states of β_2-AR (62). We first checked whether we could detect and track these nanobodies when expressed in a heterologous cell system Chinese Hamster Ovary (CHO)-K1, which lacks β_2-AR (63). We could hardly detect any of the three nanobodies in TIRF mode, as expected for background expression of a cytosolic protein (*SI Appendix*, Fig. S6 *A–G*; also see Fig. 1*M*). Importantly, coexpression of β_2-AR-YFP in these cells increased the level of detection of these three nanobodies, with Nb80-mEos2 detection increasing by 100%, Nb37-mEos2 by 30%, and Nb60-mEos2 by 1600% compared to CHO-K1 coexpressing YFP, using identical acquisition settings (*SI Appendix*, Fig. S6 *A–G*).

As these nanobodies selectively recognize unique conformations, we did not expect any mobility change following isoprenaline treatment of live cells. Indeed, isoprenaline did not alter the mobility of Nb80-mEos2 (Fig. 6 *A–D*) or Nb37-mEos2 (Fig. 6 *E–H*). Isoprenaline appears to slightly increase the mobility of Nb60-mEos (Fig. 6 *I–L*). Although the intrinsic mobility of activated receptors remained unchanged following agonist treatment, we anticipated that the proportion of activated receptors would significantly increase.

The range of mobility that overexpressed β_2-AR-YFP exhibits solely conveys the average of all conformational states. In sharp contrast, the three conformation-specific nanobodies used exhibited vastly different mobilities (Fig. 6 *C*, *G*, and *K*). Importantly, the bimodality of the diffusion coefficient distribution was unaltered, but the proportions of molecules in these immobile and mobile fractions were remarkably different (Fig. 6 *D*, *H*, and *L*). Our results confirm our earlier finding that isoprenaline reduces β_2-AR mobility (Fig. 4) and reveal that activated (Nb80) endogenous receptors are highly immobile (Fig. 6 *A–D*). The mobility of Nb60 in PC12 cells is similarly low and comparable to that of Nb60 in CHO-K1 cells coexpressing β_2-AR-YFP (*SI Appendix*, Fig. S6 *H* and *I*). Guanine nucleotide-free forms of Gαs protein (Nb37) have a relatively higher mobility (Fig. 6 *E–H*) than both Nb80 and Nb60 (inactive β_2-AR), suggesting that G-protein binding affects the clustering of the receptor. As this nanobody binds the nucleotide-free Gαs, we cannot rule out that it could bind to another endogenous activated GPCR in PC12 cells.

Conformational-specific nanobodies reveal distinct mobility patterns of active and inactive β_2-AR following inhibition of dynamin-dependent endocytosis. We demonstrated that blocking dynamin-dependent endocytosis decreases β_2-AR-YFP mobility independently of agonist-induced activation (Fig. 5). We checked whether blocking this endocytic pathway could differentially affect specific conformations of the receptor. As anticipated, dynamin inhibition decreased

the mobility of the active conformations of β_2-AR (Nb80) and Gαs (Nb37) (Fig. 7 *A–H*). Interestingly, this effect was most pronounced on the guanine nucleotide-free form of Gαs protein presumably bound to activated β_2-AR (Nb37) (Fig. 7 *E–H*) compared to that of the activated β_2-AR conformation (Nb80) (Fig. 7 *A–D*). Further, isoprenaline increased Nb80 mobility in the presence of Dyngo4a (Fig. 7 *A–D*). In contrast, Nb37 mobility decreased in the combined presence of agonist and endocytic block (Fig. 7 *E–H*). This demonstrates that both active conformations of β_2-AR (Nb80) and Gαs (Nb37) react very differently to endocytic blockade. Importantly, Dyngo4a has no effect on the mobility of the inactive receptors (Nb60) (Fig. 7 *I–L*). Strikingly, the number of trajectories detected dramatically increased upon blockade of endocytosis for active conformations of β_2-AR (Nb80) and Gαs (Nb37) (Fig. 7*M*). This supports the hypothesis that the number of receptors, and in particular activated receptors, on the plasma membrane relies on a dynamic equilibrium between activation/desensitization and sequestration. Nb80 has the lowest mobility of all tested conformations, and blocking endocytosis marginally increases its overall mobility. In contrast, Nb37 has a higher overall mobility compared to Nb80, which is decreased by isoprenaline and Dyngo4a. This suggests that blocking endocytosis reveals a tendency for activated receptors to accumulate in clusters of highly confined molecules that could represent preendocytic sites. However, both Nb80's and Nb37's interaction with β_2-AR is incompatible with β-arrestin binding, and this interaction is required to target receptors for clathrin-coated pits by subsequent AP2 and clathrin recruitment (64). A recent study shows that a prototypical class A GPCR member, β_2-AR, does not form a GPCR–G-protein–β-arrestin supercomplex to any significant degree, unlike those from the other classes (65). This suggests that two modes of immobilization occur concurrently and that the exchange required between Gαs-protein and β-arrestin binding could occur within endocytic clusters before internalization. The inactivated receptor conformation (Nb60) was also sensitive to dynamin inhibition but to a lesser extent, also suggesting some level of specificity for the activated receptors to be internalized.

Active β_2-AR forms transient nanoclusters at the plasma membrane. Active β_2-AR conformations detected using Nb80 and Nb37 have vastly different mobility at the plasma membrane. To characterize the spatiotemporal dynamic nanoclustering properties of these active conformations of β_2-AR, we performed a larger set of single-particle tracking experiments by FiLM (Fig. 8). We captured low-resolution TIRF images of the Nb80-mEos2 and Nb37-mEos2 (Fig. 8 *A* and *E*) as well as high-resolution maps of intensities (Fig. 8 *B* and *F*), diffusion coefficients (Fig. 8 *C* and *G*), and trajectories (Fig. 8 *D* and *H*). Our results revealed that activated β_2-ARs and β_2-AR–Gαs complexes are not uniformly distributed but rather organized in nanodomains on the plasma membrane (Fig. 8 *B*, *C*, *F*, and *G*). The detection density of Nb80 was lower than that of Nb37 (Fig. 8 *D* and *H*). This suggests that the proportion of activated β_2-ARs detected by Nb80 is smaller than the guanine nucleotide-free form of Gαs protein presumably bound to β_2-AR (Nb37). Intriguingly, despite their lower detection density, the Nb80-mEos2 molecules were more confined compared to Nb37 (see MSD curves and distributions of diffusion coefficients, Fig. 8 *I–L*).

Moment scaling spectrum (MSS) analysis has been widely used to characterize the mobility states of receptors at the plasma membrane (66). We therefore performed this analysis on Nb80-mEos2 and Nb37-mEos2 trajectories that lasted for at least 20 frames (0.4 s) and quantified the slope of the MSS (S_{MSS}). Depending on the values of S_{MSS}, trajectories can be categorized into immobile, confined, and freely diffusing states. We found that both Nb80-mEos2 and Nb37-mEos2 molecules displayed immobile, confined, and free diffusive motion types (Fig. 8 *M–O*). The S_{MSS} of Nb80-mEos2 trajectories was significantly lower than that of the Nb37-mEos2 trajectories (Fig. 8*M*), with a relatively larger proportion of Nb80-mEos2 molecules in the immobile and confined states and a smaller proportion in the free diffusive state compared to the Nb37-mEos2 molecules (Fig. 8 *N* and *O*).

To further characterize the mobility patterns of these two active conformations, we analyzed the Nb37-mEos2 and Nb80-mEos2 trajectories using HMM, and similarly identified three diffusive states for both Nb37-mEos2 and Nb80-mEos2 molecules: immobile (S1), intermediate (S2), and fast (S3) states. Although the apparent diffusion coefficients of these diffusive states were similar (Fig. 9 *A* and *B*), the state occupancies of Nb80-mEos2 and Nb37-mEos2 within each diffusive state were vastly different (Fig. 9*C*). The state occupancy of Nb80-mEos2 molecules in the immobile (S1) and intermediate (S2) states was significantly higher than that of Nb37-mEos2 molecules (Fig. 9*C*). Conversely, Nb37 occupancy was higher in the fast (S3) state (Fig. 9*C*). This suggests that the binding of Gαs to the activated receptor dynamically alters the proportion of time spent in each of the diffusive states, leading to an overall difference in mobility.

To assess the dynamic nature of individual nanoclusters apparent in the high-resolution images (Figs. 4 and 8), we first constructed a superresolution image of β_2-AR-YFP detected using GBP-mEos2 in live PC12 cells, depicting β_2-AR-YFP nanoclusters (*SI Appendix*, Fig. S7 *A–F*). We then used a Voronoï tessellation-based spatial clustering algorithm to identify the spatial location of the β_2-AR-YFP nanoclusters (67) (*SI Appendix*, Fig. S7 *D–F* and *Materials and Methods*). We computed the time series of molecular detections in individual nanoclusters, by time-correlated PALM (tcPALM) (68, 69), and found that the detections were highly clustered in time, indicating transient lateral trapping of β_2-AR-YFP in nanoclusters (*SI Appendix*, Fig. S7). We similarly assessed the spatiotemporal dynamics of the activated receptor species in nanoclusters using Nb80-mEos2 (Fig. 9 *D–I*) and Nb37-mEos2 (Fig. 9 *J–O*). Remarkably, superresolution images revealed nanoclusters of activated endogenous β_2-AR (Nb80) (Fig. 9*D*) and those coupled to guanine nucleotide-free form of Gαs protein (Nb37) (Fig. 9*J*) at the plasma membrane (with the caveat that Nb37 might also recognize other activated Gαs-coupled GPCRs). We could identify the locations of the nanoclusters for both activated receptor species using the Voronoï tessellation algorithm (Fig. 9 *E* and *K*). Importantly, these clusters contained high-density molecular detection as delineated in Fig. 9 *F* and *L*. Trajectories within these high-detection areas were predominantly from immobile and intermediate states as inferred by HMM (Fig. 9 *G* and *M*). When we computed the time series of molecular detections in these individual nanoclusters, we also observed transient bursts of high-frequency detections, indicating short-lived nanoclustering of β_2-AR in these activated conformational states (Fig. 9 *H* and *N*). This was more apparent in the cumulative detections of molecules, where we saw sudden changes in the detection density, indicating nanocluster assembly and disassembly events (Fig. 9 *H* and *N*). The burst duration (the apparent lifetime) of activated β_2-AR nanoclusters detected using Nb80-mEos2 was 19.2 ± 0.6 s, and using Nb37-mEos2 was 18.1 ± 0.4 s, suggesting that these nanoclusters are similarly short lived at the plasma membrane. There were detectable numbers of nanoclusters at the plasma membrane at any given point in time. These nanoclusters appeared and disappeared throughout the imaging window (Fig. 9 *H* and *N*). We computed the number of detections per burst for both Nb80-mEos2 and Nb37-mEos2 and found that they ranged between 50 and 500, and their averaged burst count was slightly over 150 (*SI Appendix*, Fig. S8 *A*, *B*, *E*, and *F*). Expectedly, the intraburst dark time, which computes the time without detection during the burst, was also similarly low for both nanobodies (0.4 s). The equivalent confinement radius for each detected burst was 90.3 ± 0.6 nm and 86.7 ± 0.4 nm for Nb80-mEos2 and Nb37-mEos2, respectively (*SI Appendix*, Fig. S8 *D* and

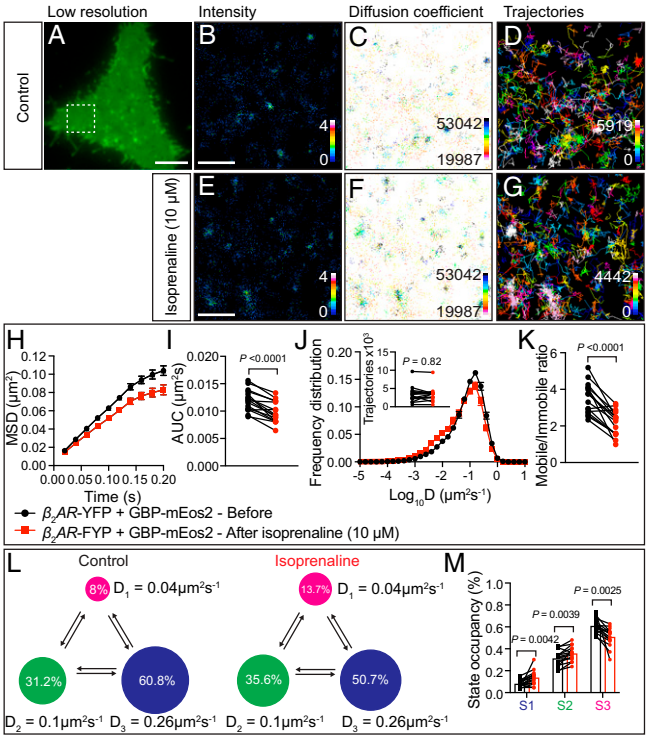

Fig. 4. Single-particle detection of β_2-*AR*-YFP by GBP-mEos2 using the FiLM technique before and after isoprenaline addition. (*A*) A representative PC12 cell in TIRF shows the green fluorescence of β_2-*AR*-YFP and GBP-mEos2 prior to photoconversion. (Scale bar, 5 μm.) (The region of interest, defined by the white box, is used for *B* and *D*).) Superresolution imaging was performed at 50 Hz and analysis of the movies generating (*B*) average intensity map; (*C*) diffusion coefficient distribution (darker colors represent lower mobility) and (*D*) trajectory map (color coded by time; warmer colors acquired later into the acquisition). (Scale bar, 1 μm.) (*E–G*) The region of interest of cell above following isoprenaline treatment (10 μM) (*E–G* as per *B–D*). (*H*) Analysis of single-particle tracking was expressed as the MSD as a function of time, (*I*) AUC, (*J*) frequency distribution of the diffusion coefficient (*Inset*: trajectory number); (*K*) mobile-to-immobile ratios (n = 16, from three independent experiments). (*L* and *M*) Hidden Markov modeling to infer mobility parameters of β_2-*AR*-YFP trajectories. (*L*) A three-state model with the inferred apparent diffusion coefficients and state occupancies are represented. Each state is illustrated by a colored circle (state 1, immobile, magenta; state 2, intermediate, green; state 3, fast mobile, blue), with the area proportional to the state occupancy. (*M*) Comparison of state occupancies inferred from β_2-*AR*-YFP trajectories (n = 16 sets, 16 cells from three independent experiments). Statistics of the AUC, mobile-to-immobile ratio, and state occupancy were performed using a paired Student's *t* test, and trajectory number comparison was made using paired nonparametric Wilcox test.

H). Considering the high similarity of nanoclustering dynamics displayed by Nb80 and Nb37, it is likely that the latter conveys useful insight into the dynamic of activated Gαs-coupled β_2-AR.

Taken together, these findings suggest that agonist treatment promotes an increase in recycling of activated β_2-AR and an increase in Gαs-protein coupling, leading to increased clustering and decreased mobility of the receptor. Overall, FiLM can be used in association with purpose-designed selective nanobodies to quantify the single-molecule dynamics of endogenous proteins at the plasma membrane in specific conformations.

Discussion

In this study, we have expressed single-domain nanobodies in cultured cells and in vivo to visualize the dynamic nanocluster organization of endogenous proteins. We first used single-molecule imaging of intracellularly expressed GFP binding nanobodies tagged with mEos2 to characterize the nanoscale organization of several GFP proteins in multiple cell lines and two widely used small animal models as proof-of-concept. We then applied this nanobody-based single-molecule imaging approach to track endogenous β_2-AR in highly defined conformations (activated, bound to Gαs, and inactivated) and discovered common mobility states associated which all of these conformations and specific changes in the time spent within each of these states.

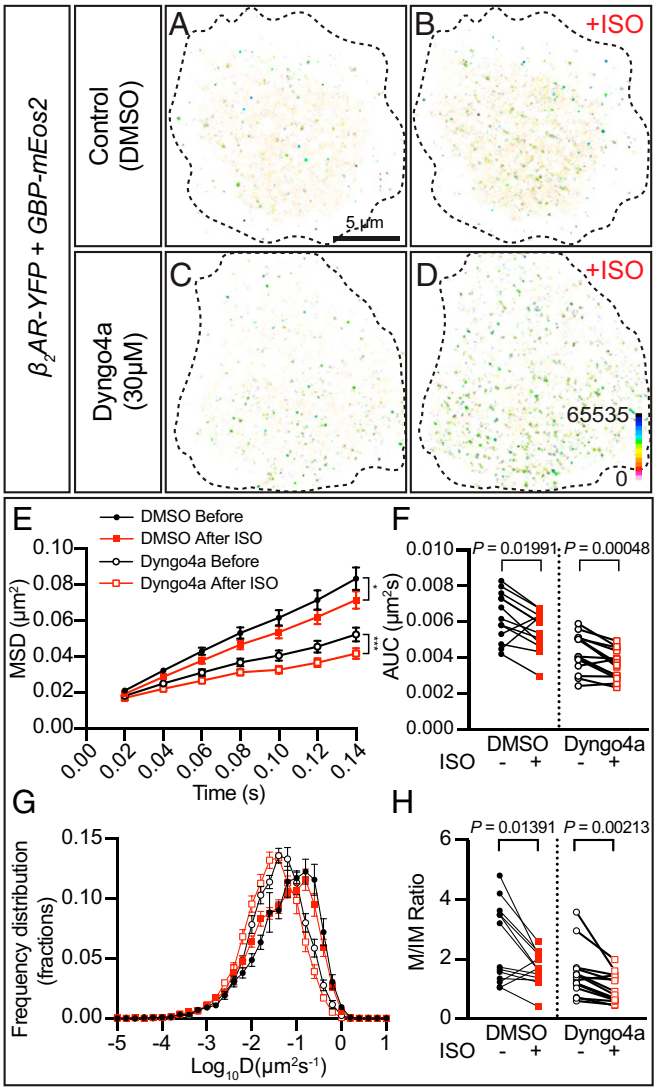

Fig. 5. Single-particle detection of β_2-AR-YFP by GBP-mEos2 following dynamin inhibition with Dyngo4a before and after isoprenaline treatment. Cells were transfected with β_2-AR-YFP and GBP-mEos2 and pretreated with either DMSO or 30 μM Dyngo4a 20 min prior to imaging before and after 10 μM isoprenaline treatment. (*A* and *B*) A DMSO-treated representative PC12 cell depicting the diffusion coefficient distribution of all $_2$-*AR* tracked receptors is shown (*A*) before and (*B*) following isoprenaline treatment (10 μM) (outline of cell is shown in black dotted line). (*C* and *D*) A representative cell pretreated with Dyngo4a is shown (*C*) before and (*D*) after isoprenaline treatment. (Scale bar, 5 μm.) (*E*) Analysis of single-particle tracking was expressed as the MSD as a function of time, (*F*) AUC, (*G*) frequency distribution of the diffusion coefficient, and (*H*) mobile-to-immobile ratios (n = 13 [DMSO] and 15 [Dyngo4a], from three independent experiments). Statistics of the AUC were performed using a paired Student's *t* test. Analysis of the mobile to immobile ratio was performed using a paired Wilcoxon test.

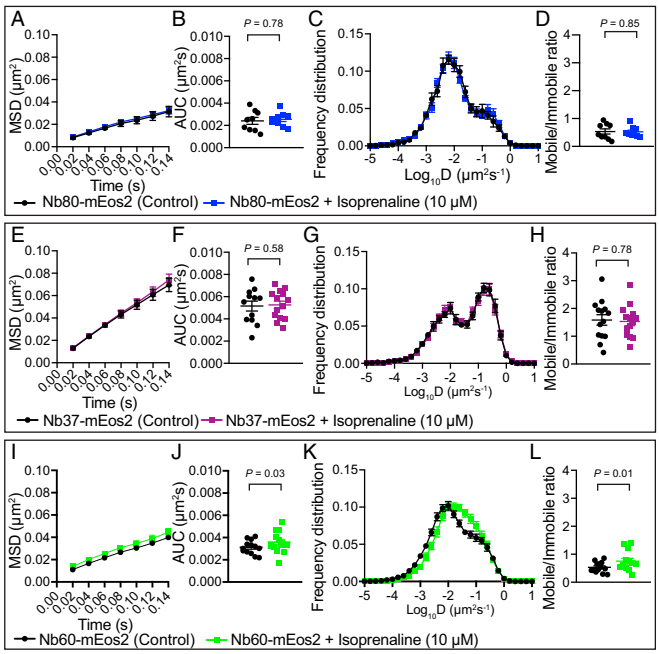

Fig. 6. FiLM of Nb80-mEos2, Nb37-mEos2, and Nb60-mEos2 in PC12 cells following isoprenaline treatment. Transfected PC12 cells expressing (*A–D*) Nb80-mEos2, (*E–H*) Nb37-mEos2, or (*I–L*) Nb60-mEos2 were imaged and subjected to live FiLM. Cells were imaged before and after isoprenaline treatment (10 μM). Superresolution imaging was performed at 50 Hz. Movies were analyzed and data expressed as (*A*, *E*, and *I*) MSD as a function of time, (*B*, *F*, and *J*) AUC, (*C*, *G*, and *K*) frequency distribution of the diffusion coefficient, and (*D*, *H*, and *L*) mobile-to-immobile ratio (n = 9, 14, and 13, cells, respectively, for each condition from three independent experiments). Statistical analysis of the AUC and mobile-to-immobile ratio was performed using a paired Student's t test.

Expressing GBP-mEos2 in combination with existing GFP expression constructs or transgenic strains provides a fast and efficient way to perform single-particle tracking in cells and living organisms. In this study, we have highlighted examples of GBP-mEos2 imaging in the muscle fibers of zebrafish and the PLM mechanosensory neurons of *C. elegans*. This was achieved by injection of RNA/plasmid DNA in vivo. In these two systems, we were able to optically penetrate through to the region of interest by adapting an imaging technique previously used to image Syntaxin-mEos2 at the neuromuscular junction of *Drosophila melanogaster* larvae (6). As the nematode strains that were imaged exhibited a roller phenotype caused by the transgenic marker, which caused the animals to rotate on their longitudinal axis as they moved, the orientation of the PLM neurons often changed between samples. In circumstances where the PLM neuron was in a higher z dimension due to the animal's rotation, we were also able to use ultrahigh-power TIRF on our microscopy system. The generation of stable transgenic strains that express GBP-mEos2 ubiquitously, or in a tissue-specific manner, could facilitate crosses with existing GFP-expressing strains, and streamline the use of this technique for superresolution imaging in a large range of GFP animal models. In our cellular systems, where the cells were attached to the glass-bottom dishes, imaging could be achieved using TIRF illumination.

In order to minimize the possibility of tracking unbound GBP-mEos2 cytosolic molecules, we eliminated trajectories from molecules that were detected in fewer than eight frames (160 ms) (the likelihood of detecting a freely diffusible molecule in the TIRF plane is very low), and, when processing our single-particle tracking data, we used conservative thresholding. To avoid artifacts from connecting distinct molecules, a maximum distance threshold of 0.318 μm between subsequent single-molecule localizations was applied. Using these settings, we were able to demonstrate that sptPALM and FiLM give rise to indistinguishable results, suggesting that the contribution of unbound GBP was negligible within the constraints of our acquisition settings. There are several other ways in which the contributions of background unbound GBP-mEos2 could be minimized. We demonstrated that the "destabilized" GBP nanobodies (37), in which the unbound nanobody is unstable and degraded, showed identical mobility using the abovementioned tracking parameters. Alternatively, genetically encoded nanobodies/biosensors could be generated in cellular systems within the same endogenous promoter as its target protein using the CRISPR-Cas9 system, and achieve equal expression of the nanobody and its target. Finally, overexpression artifacts can also be overcome by expression of a biosensor using a transcriptional system that matches the expression of its target protein (70).

Biological Insights Using GBP-mEos2 Imaging. Using both sptPALM and FiLM, we demonstrated that most PH-PLCδ molecules are highly mobile on the plasma membrane, with only a small fraction being confined in nanoclusters. The reversible trapping of PH-PLCδ in nanoclusters favors dynamic fluctuations in the nanoscale organization of the plasma membrane and the rapid exchange of the molecular components of nanoclusters (71, 72). Similarly, we observed that phospholipase PA-PLA1 exhibited a

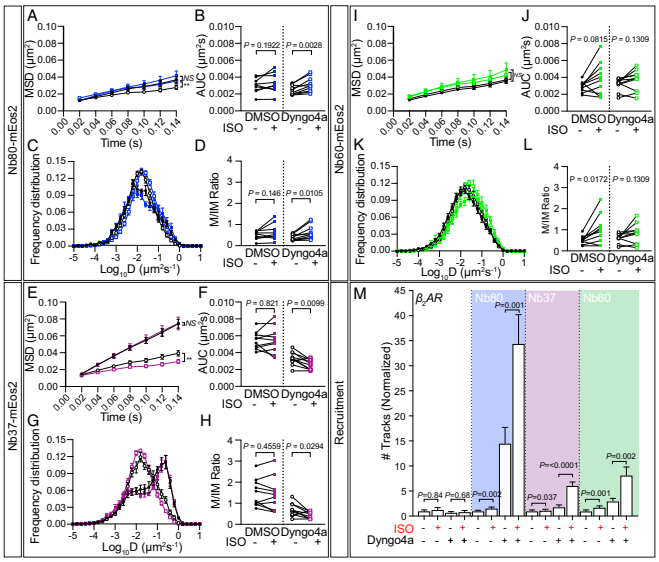

Fig. 7. Single-particle detection of endogenous β_2-AR by Nb80-mEos2, Nb37-mEos2, and Nb60-mEos2 following dynamin inhibition with Dyngo4a before and after isoprenaline treatment. Transfected PC12 cells expressing (*A–D*) Nb80-mEos2, (*E–H*) Nb37-mEos2, or (*I–L*) Nb60-mEos2 were imaged and subjected to live FiLM. Cells were pretreated with either DMSO or Dyngo4a (30 μM) for 20 min, then imaged before and after isoprenaline treatment (10 μM). Superresolution imaging was performed at 50 Hz. Movies were processed and single particle tracking was analyzed and represented as (*A*, *E*, and *I*) MSD as a function of time, (*B*, *F*, and *J*) AUC, (*C*, *G*, and *K*) frequency distribution of the diffusion coefficient, and (*D*, *H*, and *L*) mobile-to-immobile ratio (M/IM). (N [DMSO] = 9, 10, and 10 cells, respectively, and N [Dyngo4a] = 10, 11, and 10 from three to four independent experiments). Statistical analysis of the AUC and mobile-to-immobile ratio was performed using a paired Student's t test, with the exception of Nb60 Dyngo4a results, which were analyzed by paired Wilcoxon test. (*M*) Number of trajectories from each 16,000-frame movie was analyzed to estimate the change in trajectories upon Dyngo4a and isoprenaline treatment. Paired Student's t test was used to compare the number of trajectories before and after isoprenaline treatment.

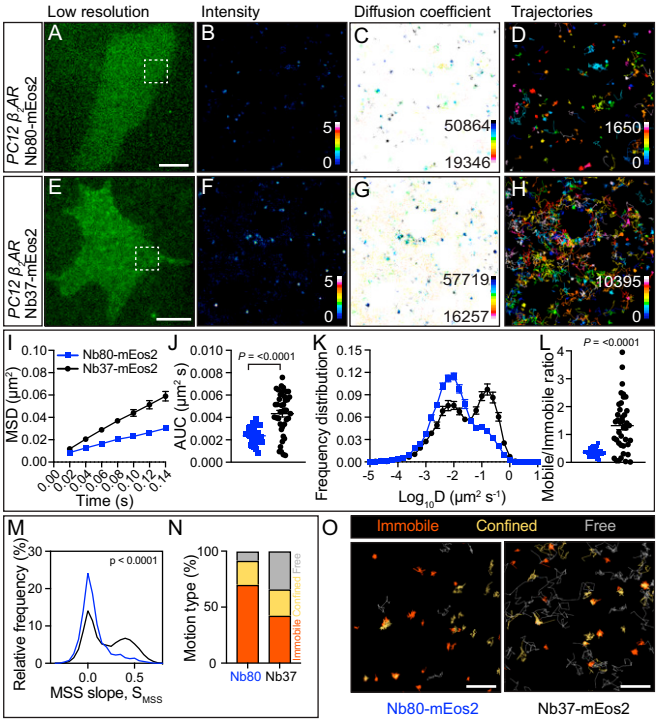

Fig. 8. Single-particle detection of Nb80-mEos2 and Nb37-mEos2 in PC12 cells using the FiLM technique. (*A*) Representative PC12 cell, in TIRF, of the green fluorescent Nb80-mEos2 intrabody that targets the active conformation of β_2-AR taken prior to photoconversion with a 405-nm laser. (Scale bar, 5 μm.) The region of interest is defined by the white box in *A* Super-resolution imaging was performed at 50 Hz, and analysis of movies generated (*B*) average intensity map, (*C*) diffusion coefficient map distribution (darker colors represent lower mobility), and (*D*) trajectory map (color coded by time; warmer colors acquired later into the acquisition). (*E*) PC12 cell expressing Nb37-mEos2 (*E–H* as per *A–D*). Analysis of single-particle tracking was expressed as the (*I*) MSD as a function of time, (*J*) AUC, (*K*) frequency distribution of the diffusion coefficient, and (*L*) mobile-to-immobile ratio (N = 31 and 41 cells for Nb80 and Nb37, respectively). Statistics of AUC and mobile-to-immobile ratio were performed using a Student's t test. (*M*) Distribution of the moment scaling slope of trajectories (n = 6,291 Nb80-mEos2 trajectories from 31 cells and 17,841 Nb37-mEos2 trajectories from 41 cells). (*N*) Percentage of immobile, confined, and free motion type identified using MSS. (*O*) Trajectories annotated based on different motion types. (Scale bar, Nb80, 1 μm; Nb37, 0.7 μm.)

large proportion of highly mobile molecules at the plasma membrane and only a few highly dynamic nanoclusters.

Caveolae are Ω-shaped invaginations on the plasma membrane which are involved in endocytosis and transcytosis (73, 74). Analysis of the mobility of Cav1 and Cav3 molecules revealed a predominantly slow diffusive population and a relatively small freely diffusing population. This is in agreement with a previous report (75). The freely diffusing mobile population undergoes a rapid and continuous exchange cycle with the plasma membrane. We found that the mobility patterns of Cav1 in MDCK cells and Cav3 in zebrafish muscle fibers were highly similar. Subtle differences could be attributed to the cellular system itself or to a slightly different range of binding interactors. Interestingly, many trajectories from both systems exhibited periods of confinement separated by free diffusion (dual confinement), suggesting that a small population of Cav molecules can shuttle between caveolae. It is important to note that, due to the highly clustered nature of Cav in caveolae, decreased efficiency of nanobody binding could potentially occur and contribute to that effect. Density must therefore be considered when interpreting mobility change. In addition, the different Cav isotypes could have differences in the rate of assembly and budding off, and thus exhibit varying lifetime duration on the plasma membrane (76).

Using GBP-mEos2, we also characterized the nanoscale organization of EFF-1, a key *C. elegans* membrane fusogen involved in a variety of cell–cell fusion events, as well as neurite self-fusion during remodeling and repair (46–49). In particular, following axotomy of the PLM neuron, EFF-1 allows the regrowing axon to contact and fuse with its own separated axonal fragment. Understanding the precise mechanism underpinning this essential property is paramount to generating novel therapies to reestablish functional regeneration after nervous system injury. Our data show that EFF-1 is relatively immobile in intact axons, a finding that is in agreement with a report of its presence in slow-moving intracellular vesicles such as early endosomes (77). However, we also demonstrate that EFF-1 has a small mobile component, which is likely to reflect some of the plasma membrane molecules. Assessment of how the nanoscale organization of EFF-1 is affected on the plasma membrane during the repair process would make an interesting target for further study using FiLM.

Nanoclustering Dynamics of Activated Endogenous β_2-ARs. As nanobody applications broaden, the increasing repertoire of nanobody libraries offers unique opportunities to unravel the nanoscale organization of many essential molecules. In addition, the ability of nanobodies to facilitate structural studies provides even more opportunities to utilize these existing conformation-specific nanobodies for single-molecule imaging studies. The use of conformation-specific nanobodies against β_2-AR allowed us to differentiate conformationally distinct subpopulations and determine their mobility and clustering dynamics. We revealed that agonist-induced activation of β_2-AR-YFP decreases its mobility, leading to clustering. We revealed that a small subpopulation of endogenous activated β_2-AR recognized by Nb80 are highly immobile compared to expressed β_2-AR-YFP which encompasses the entire repertoire of β_2-AR conformations. This activated conformation, that precedes G-protein coupling, is theorized to represent a transient high-energy state (60, 78, 79). Our data demonstrate that this population has the lowest mobility of any of the tested conformations. Our results also confirm that GPCRs form nanoclusters/hotspots on the plasma membrane, as recently demonstrated (52, 80). These nanobodies are therefore able to capture subtle changes to the nanoscale organization of endogenous activated β_2-ARs conformations which could not be fully elucidated using the overexpressed receptor. We demonstrated that the active β_2-AR conformations detected by different nanobodies (Nb80 and Nb37) did not change mobility upon agonist treatment. This suggests that the immobilization of β_2-AR-YFP elicited by isoprenaline likely stems from changes in the proportion of receptors in activated conformations. We further show that the activated state of β_2-AR (Nb80) forms transient nanoclusters that likely represent platforms on which transducer–effector binding can occur.

Following activation, the Gαs subunit associates with the activated β_2-AR to mediate effector binding. The Nb37 nanobody interacts with the Gαs subunit in its nucleotide-free form and acts as a biosensor of Gαs-coupled GPCR including β_2-AR. We found that the mobility of Nb37 was significantly higher than the purely active (Nb80) or inactive conformations (Nb60). Using MSS and HMM, we identified a larger proportion of Nb37 molecules in freely diffusive state compared to Nb80 molecules. Increase in freely diffusing molecules could potentially favor exit from Nb80 positive nanoclusters. Such lateral exclusion could also be important to regulate the timing of the signaling platforms on the plasma membrane and help generate endocytic hotspots mediating subsequent internalization, as recently described (52). A correlation between Gαs association and actin destabilization has recently been found to occur upon activation of the Serotonin receptor 1a—another GPCR (81). This could therefore represent a conserved mechanism by which the mobility of the G-protein–linked activated receptors is modulated.

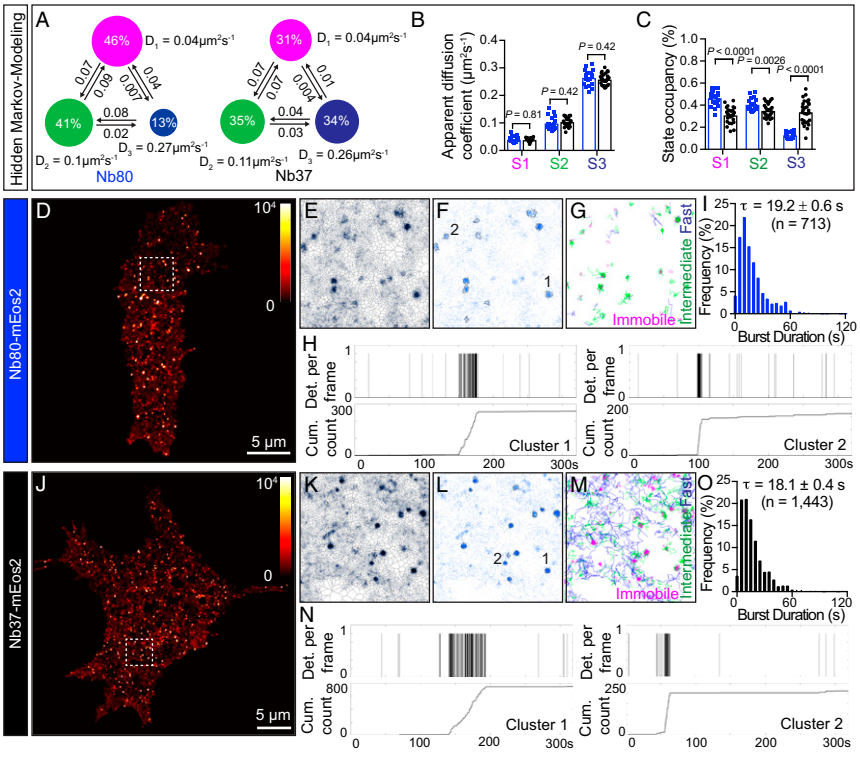

Fig. 9. Dynamics properties of endogenous activated β_2-AR and Gαs-coupled GPCR nanoclusters. (*A–C*) Individual trajectories of the single-particle tracking data of Nb80-mEos2 and Nb37-mEos2 were analyzed using HMM to infer mobility parameters. (*A*) A three-state model with the inferred apparent diffusion coefficients and state occupancies represented. Each state is illustrated by a colored circle (state 1, immobile, magenta; state 2, intermediate, green; state 3, fast mobile, blue), with the area proportional to the state occupancy. (*B*) Comparison of apparent diffusion coefficients of each state inferred from Nb80-mEos2 and Nb37-mEos2 trajectories. (*C*) Comparison of state occupancies inferred from Nb80-mEos2 and Nb37-mEos2 trajectories (n = 28 sets, 34 cells for Nb37-mEos2, n = 19 sets, 31 cells for Nb80-mEos2). Statistics of apparent diffusion coefficient and state occupancy were performed using a Student's t test with Welch's correction. (*D–N*) The dynamics of individual nanoclusters assessed using a combination of Voronoï-based cluster detection and tcPALM analyses in live PC12 cells. (*D* and *J*) Representative superresolution images of (*D*) Nb80-mEos2 and (*J*) Nb37-mEos2. (*E* and *K*) Voronoï diagrams of (*E*) Nb80-mEos2 and (*K*) Nb37-mEos2 detections. (*F* and *L*) Nanoclusters (black outline) detected by (*F*) Nb80-mEos2 and (*L*) Nb37-mEos2 were identified using Voronoï-based tessellation algorithm. (*G*) Nb80-mEos2 and (*M*) Nb37-mEos2 trajectories displaying immobile, intermediate, and fast motion patterns inferred using HMM. (*H* and *N*) Representative time series of detections from β_2-AR nanoclusters detected using (*H*) Nb80-mEos2 and (*N*) Nb37-mEos2. (*I* and *O*) The distribution of apparent burst times of (*I*) Nb80-mEos2 and (*O*) Nb37-mEos2 nanoclusters.

Previous studies have shown that "puncta" of Nb80-GFP associating with the membrane in TIRF did not colocalize with endocytic machinery (including the Clathrin-LC), suggesting they do not associate with endocytic platforms, but rather reassociated with early endosomes in a second phase of recruitment and signaling (29). We observed an accumulation of activated receptors at the plasma membrane upon blockade of endocytosis, and a dramatic reduction of its mobility. Importantly, this effect was most robust on the activated receptor populations (Nb80 and Nb37). These results suggest that these receptors are constantly being internalized and that the activated species are selectively targeted for endocytosis upon agonist stimulation. Although we cannot rule out potential off-target effects of the dynamin inhibitor used (Dyngo4a), it is the most relevant acute treatment to efficiently block dynamin-dependent endocytosis (82).

These nanoclusters are likely to represent signaling hubs that accumulate on the plasma membrane when endocytosis is blocked, but are not necessarily associated with the endocytic event. The accumulation of active conformations during endocytic block suggests that compensatory endocytosis may serve as a mechanism by which the β_2-AR conformations are kept in a state of equilibrium, allowing the membrane overall β_2-AR population to remain constant and ready to receive further signaling input balanced with a level of desensitization to curb excessive cAMP downstream events.

How long these nanoclusters remain biologically active is currently unknown. We used a Voronoï tessellation-based spatial clustering algorithm and computed the time series of molecular detections in individual nanoclusters to assess the temporal dynamics of nanoclusters containing endogenous β_2-AR in activated conformations. This revealed that activated receptors are transiently trapped in "hotspot" regions of the plasma membrane, defining individual nanoclusters. We observed these clusters to intermittently appear and disappear on the plasma membrane throughout the acquisition and have an approximate duration of 20 s. The density of detection within these discrete regions is sporadic before and after, but sharply (albeit transiently) increases during this 20-s time window. Moreover, the mobility of these molecules is also highly reduced within these regions during this time window. These nanoclusters are therefore short lived, which may regulate efficient receptor desensitization and signal duration. Further understanding the mechanism affecting the temporal dynamics of GPCR nanoclustering is needed to fully unveil this new regulatory function of transient nanoclustering in signaling.

The use of purpose-designed nanobodies with specific affinities for biologically relevant conformations of endogenous proteins allowed us to use FiLM to unravel the dynamics of endogenous β_2-AR undergoing specific interactions. More generally, we demonstrated the equivalence of superresolution data acquired using photoconvertible tagged nanobodies to a GFP-labeled protein versus the photoconvertible tagged protein itself, showing the potential to use FiLM to study the membrane dynamics of a wide range of available GFP-labeled proteins without requiring extensive recloning. FiLM can also potentially be expanded to encompass other intrabodies and other biosensors (83–86), and the use of alternative tags such as HALO and SNAP (87, 88). As with all superresolution techniques, careful optimization of sample preparation and washing, selection of the most appropriate fluorescent ligands (89), and optimization of data acquisition and processing are crucial. Further, interpretation of the results should take into consideration whether the nanobody is interfering with the given biological process studied. Taking these considerations into account, FiLM provides a platform with which to study the mobility of intracellular GFP-tagged and endogenous proteins in selective conformations using superresolution single-molecule tracking in cultured cells and animal models.

Materials and Methods

PC12 Cell Culture and Transfection. Pheochromocytoma (PC12) cells were maintained at 37 °C and 5% CO_2 in Dulbecco's modified Eagle's medium

(DMEM) supplemented with 5% fetal calf serum (FCS) (Bovogen), 5% heat-inactivated horse serum (Gibco, Invitrogen) and 0.5% GlutaMAX (Gibco, Invitrogen). Cells were transfected using Lipofectamine LTX and Plus reagent according to the manufacturer's instructions (Thermofisher Scientific). For plasmids and detailed information, see *SI Appendix*.

MDCK Cell Culture and Transfection. MDCK cells were maintained as previously described (90). The cells were grown in DMEM/F-12 (Life Technologies) supplemented with 10% FCS and 2 mM L-glutamine. Cav1 constructs were tagged with mEos2, a kind gift from Katharina Gaus, University of New South Wales, Sydney, Australia. Tagged constructs were transfected using Lipofectamine 2000 reagent (Life Technologies) as per the manufacturer's instructions.

***C. elegans* Strains and Imaging Conditions.** Nematodes were cultured under standard conditions (91). Experiments were performed on L3/L4-stage hermaphrodites raised at 22 °C. Prior to imaging, transgenic animals were washed to remove excess bacteria by transferal, via a platinum wire, through successive 20-μL drops of M9 buffer for ∼15 min per wash. The animals were then transferred into a 10-μL drop of M9 buffer containing 0.05% tetramisole hydrochloride onto a 4% agar pad prepared on an 18-mm no. 1.5 glass coverslip. Once the animals were anesthetized, the coverslip (containing the animals) was carefully inverted, using tweezers, onto a 29-mm Petri dish with a 20-mm glass bottom (In Vitro Scientific), with a ∼5-μL drop of 0.05% tetramisole hydrochloride in M9 buffer. For generation of plasmids for *C. elegans* experiments, see *SI Appendix*.

The strains used were QH6853[*vdEx1724(Pmec-4::eff-1::mEos2)* + *rol-6(su1006)*], QH6854[*vdEx1725(Pmec-4::eff-1::mEos2)* + *rol-6(su1006)*], QH6488 [*vdEx1522(Pmec-4::eff-1::gfp+Pmec-4::mEos2-N1-GBP-Nb)* + *rol-6(su1006)*], and QH6490[*vdEx1524(Pmec-4::eff-1::gfp* + *Pmec-4::mEos2-N1-GBP-Nb)* + *rol-6(su1006)*].

In Vivo Imaging of Zebrafish. The 48- and 72-hpf larvae were manually dechorionated and anesthetized using ethyl 3-aminobenxoate methanesulfonate (tricaine), as previously described (92). Animals were embedded alive in 1.5% low-melting agarose supplemented with tricaine and mounted on coverglass–bottomed dishes. E3 medium supplemented with tricaine was added to the top of the agarose prior to imaging. For Zebrafish maintenance and transgenic lines, generation of plasmids for zebrafish experiments, and RNA synthesis and injections in zebrafish, see *SI Appendix*.

FiLM and sptPALM. For live-cell TIRF imaging, transfected cells were visualized on a Roper Scientific TIRF microscope equipped with an iLas^2 double laser illuminator (Roper Scientific), a Nikon CFI Apo TIRF 100×/1.49 NA oil-immersion objective, and an Evolve 512 Delta EMCCD camera (Photometrics). Image acquisition was performed using MetaMorph software (version 7.7.8, Molecular Devices). Cells were bathed in Buffer A (145 mM NaCl, 5 mM KCl, 1.2 mM Na_2HPO_4, 10 mM D-glucose, 20 mM Hepes, pH 7.4). Time-lapse TIRF movies were captured at 50 Hz (20-ms exposure per frame) at 37 °C. For sptPALM, a Stradus 405-nm laser (Vortan Laser Technology) was used to photoactivate the cells expressing mEos2-tagged constructs, and a Jive 561-nm laser (Cobolt Lasers) was used for excitation of the resulting photoconverted single-molecule fluorescence signal. The sample was illuminated simultaneously with both the lasers. To isolate the mEos2 signal from autofluorescence and background signals, we used a double beam splitter (LF488/561-A-000, Semrock) and a double band emitter (FF01-523/610-25, Semrock). To spatially distinguish and temporally separate the stochastically activated molecules during acquisition, the power of the lasers was adjusted, such that the 405-nm laser used 1 to 2% of the initial laser power (4 mW at the sample plane, from 100 mW out of the laser head), and the 561-nm laser used 75 to 80% of the full laser power (22 mW at the sample plane, from 150 mW out of the laser head). For imaging of live organisms and single-particle tracking data analysis, see *SI Appendix*.

Data Availability. All processed data will be made available upon request and in The University of Queensland data repository, UQ eSpace (https://doi.org/10.14264/03a862c). Plasmids will also be deposited to Addgene (https://www.addgene.org/) upon publication, with the exception of Nb80 and Nb37 which are available upon request to the Steyaert Lab by emailing mta.requests@vib.be.

ACKNOWLEDGMENTS. We acknowledge the use of the Microscopy Australia Facility at the Centre for Microscopy and Microanalysis at The University of Queensland. We thank Rowan Tweedale for critical appraisal of the manuscript, Jake Carrol and the IT department at the Queensland Brain Institute (QBI), Rumelo Amor, and all past and present members of the Advanced Microscopy and Microanalysis Facility at QBI for their outstanding microscopy support. We thank Daniel Choquet and J. B. Sibarita for invaluable discussions about this project. We thank Professor Mark von Zastrow for providing the Nb80 nanobody, and Associate Professor Brett Collins for thoughtful discussion, providing the GBP, and creating molecular illustrations within Figs. 1 and 2. The work was supported by Australian Research Council (ARC) Discovery Project Grant DP170100125; ARC Linkage Infrastructure Equipment and Facilities Grant LE130100078; National Health and Medical Research Council (NHMRC) Senior Research Fellowship 1155794 to F.A.M., NHMRC Project Grant 1129367 and NHMRC Senior Research Fellowship 1111042 to M.A.H., and NHMRC-ARC Dementia Research Development Fellowship 1108489 to S.C.; Academia of Finland Postdoctoral Research Fellowship 298124 and an ARC Discovery Early Career Researcher Award (DE190100565) to M.J.; University of Queensland Postdoctoral Research Fellowship to P.P.; NHMRC Project Grants 1037320 and 1058565 and an ARC Centre of Excellence in Convergent Bio-Nano Science and Technology to R.G.P.; and NHMRC Investigator Grant 1174145, NHMRC Project Grant 1165850, and a Rebecca L. Cooper Medical Research Project Grant PG2019405 to J.G. Nb80, Nb37, and Nb60 were discovered in the J.S. laboratory. E.P. and J.S. thank INSTRUCT, part of the European Strategy Forum on Research Infrastructures and the Research Foundation–Flanders, for support of the nanobody discoveries.

1. E. Betzig *et al*., Imaging intracellular fluorescent proteins at nanometer resolution. *Science* **313**, 1642–1645 (2006).
2. S. T. Hess, T. P. Girirajan, M. D. Mason, Ultra-high resolution imaging by fluorescence photoactivation localization microscopy. *Biophys. J.* **91**, 4258–4272 (2006).
3. B. Huang, H. Babcock, X. Zhuang, Breaking the diffraction barrier: Super-resolution imaging of cells. *Cell* **143**, 1047–1058 (2010).
4. S. Manley *et al*., High-density mapping of single-molecule trajectories with photoactivated localization microscopy. *Nat. Methods* **5**, 155–157 (2008).
5. M. J. Rust, M. Bates, X. Zhuang, Sub-diffraction-limit imaging by stochastic optical reconstruction microscopy (STORM). *Nat. Methods* **3**, 793–795 (2006).
6. A. T. Bademosi *et al*., In vivo single-molecule imaging of syntaxin1A reveals polyphosphoinositide- and activity-dependent trapping in presynaptic nanoclusters. *Nat. Commun.* **8**, 13660 (2017).
7. R. Kasula *et al*., The Munc18-1 domain 3a hinge-loop controls syntaxin-1A nanodomain assembly and engagement with the SNARE complex during secretory vesicle priming. *J. Cell Biol.* **214**, 847–858 (2016).
8. B. Bolognesi, B. Lehner, Reaching the limit. *eLife* **7**, e39804 (2018).
9. T. J. Gibson, M. Seiler, R. A. Veitia, The transience of transient overexpression. *Nat. Methods* **10**, 715–721 (2013).
10. M. Arbabi-Ghahroudi, Camelid single-domain antibodies: Historical perspective and future outlook. *Front. Immunol.* **8**, 1589 (2017).
11. E. Beghein, J. Gettemans, Nanobody technology: A versatile toolkit for microscopic imaging, protein-protein interaction analysis, and protein function exploration. *Front. Immunol.* **8**, 771 (2017).
12. M. H. Kubala, O. Kovtun, K. Alexandrov, B. M. Collins, Structural and thermodynamic analysis of the GFP:GFP-nanobody complex. *Protein Sci.* **19**, 2389–2401 (2010).
13. U. Rothbauer *et al*., Targeting and tracing antigens in live cells with fluorescent nanobodies. *Nat. Methods* **3**, 887–889 (2006).
14. G. Giannone, E. Hosy, J. B. Sibarita, D. Choquet, L. Cognet, High-content super-resolution imaging of live cell by uPAINT. *Methods Mol. Biol.* **950**, 95–110 (2013).
15. J. Ries, C. Kaplan, E. Platonova, H. Eghlidi, H. Ewers, A simple, versatile method for GFP-based super-resolution microscopy via nanobodies. *Nat. Methods* **9**, 582–584 (2012).
16. D. Albrecht, C. M. Winterflood, H. Ewers, Dual color single particle tracking via nanobodies. *Methods Appl. Fluoresc.* **3**, 024001 (2015).
17. G. Giannone *et al*., Dynamic superresolution imaging of endogenous proteins on living cells at ultra-high density. *Biophys. J.* **99**, 1303–1310 (2010).
18. D. Nair *et al*., Super-resolution imaging reveals that AMPA receptors inside synapses are dynamically organized in nanodomains regulated by PSD95. *J. Neurosci.* **33**, 13204–13224 (2013).
19. M. Joensuu *et al*., Subdiffractional tracking of internalized molecules reveals heterogeneous motion states of synaptic vesicles. *J. Cell Biol.* **215**, 277–292 (2016).
20. D. P. Buser, K. D. Schleicher, C. Prescianotto-Baschong, M. Spiess, A versatile nanobody-based toolkit to analyze retrograde transport from the cell surface. *Proc. Natl. Acad. Sci. U.S.A.* **115**, E6227–E6236 (2018).
21. M. Joensuu *et al*., Visualizing endocytic recycling and trafficking in live neurons by subdiffractional tracking of internalized molecules. *Nat. Protoc.* **12**, 2590–2622 (2017).
22. C. Hamers-Casterman *et al*., Naturally occurring antibodies devoid of light chains. *Nature* **363**, 446–448 (1993).
23. T. De Meyer, S. Muyldermans, A. Depicker, Nanobody-based products as research and diagnostic tools. *Trends Biotechnol.* **32**, 263–270 (2014).
24. P. D. Kaiser, J. Maier, B. Traenkle, F. Emele, U. Rothbauer, Recent progress in generating intracellular functional antibody fragments to target and trace cellular components in living cells. *Biochim. Biophys. Acta* **1844**, 1933–1942 (2014).
25. S. Muyldermans, Nanobodies: Natural single-domain antibodies. *Annu. Rev. Biochem.* **82**, 775–797 (2013).

26. T. Vercruysse, E. Pardon, E. Vanstreels, J. Steyaert, D. Daelemans, An intrabody based on a llama single-domain antibody targeting the N-terminal alpha-helical multimerization domain of HIV-1 rev prevents viral production. *J. Biol. Chem.* **285**, 21768–21780 (2010).
27. J. M. Tremblay *et al*., Camelid single domain antibodies (VHHs) as neuronal cell intrabody binding agents and inhibitors of Clostridium botulinum neurotoxin (BoNT) proteases. *Toxicon* **56**, 990–998 (2010).
28. P. Várnai, T. Balla, Visualization of phosphoinositides that bind pleckstrin homology domains: Calcium- and agonist-induced dynamic changes and relationship to myo-[3H]inositol-labeled phosphoinositide pools. *J. Cell Biol.* **143**, 501–510 (1998).
29. R. Irannejad *et al*., Conformational biosensors reveal GPCR signalling from endosomes. *Nature* **495**, 534–538 (2013).
30. S. G. Rasmussen *et al*., Structure of a nanobody-stabilized active state of the β(2) adrenoceptor. *Nature* **469**, 175–180 (2011).
31. S. G. Rasmussen *et al*., Crystal structure of the β2 adrenergic receptor-Gs protein complex. *Nature* **477**, 549–555 (2011).
32. D. P. Staus *et al*., Allosteric nanobodies reveal the dynamic range and diverse mechanisms of G-protein-coupled receptor activation. *Nature* **535**, 448–452 (2016).
33. N. Ariotti *et al*., Modular detection of GFP-labeled proteins for rapid screening by electron microscopy in cells and organisms. *Dev. Cell* **35**, 513–525 (2015).
34. J. Wang, D. A. Richards, Segregation of PIP2 and PIP3 into distinct nanoscale regions within the plasma membrane. *Biol. Open* **1**, 857–862 (2012).
35. A. Kechkar, D. Nair, M. Heilemann, D. Choquet, J. B. Sibarita, Real-time analysis and visualization for single-molecule based super-resolution microscopy. *PLoS One* **8**, e62918 (2013).
36. N. Ariotti *et al*., Ultrastructural localisation of protein interactions using conditionally stable nanobodies. *PLoS Biol.* **16**, e2005473 (2018).
37. J. C. Tang *et al*., Detection and manipulation of live antigen-expressing cells using conditionally stable nanobodies. *eLife* **5**, e15312 (2016).
38. W. Shimoi *et al*., p125 is localized in endoplasmic reticulum exit sites and involved in their organization. *J. Biol. Chem.* **280**, 10141–10148 (2005).
39. M. Drab *et al*., Loss of caveolae, vascular dysfunction, and pulmonary defects in caveolin-1 gene-disrupted mice. *Science* **293**, 2449–2452 (2001).
40. C. Minetti *et al*., Impairment of caveolae formation and T-system disorganization in human muscular dystrophy with caveolin-3 deficiency. *Am. J. Pathol.* **160**, 265–270 (2002).
41. A. T. Bademosi *et al*., In vivo single-molecule tracking at the *Drosophila* presynaptic motor nerve terminal. *J.Vis. Exp.*, e56952 (2018).
42. T. E. Hall, N. Martel, H. P. Lo, Z. Xiong, R. G. Parton, A plasmid library of full-length zebrafish rab proteins for *in vivo* cell biology. *Cell. Logist.* **7**, e1301151 (2017).
43. D. S. Park *et al*., Caveolin-1/3 double-knockout mice are viable, but lack both muscle and non-muscle caveolae, and develop a severe cardiomyopathic phenotype. *Am. J. Pathol.* **160**, 2207–2217 (2002).
44. W. A. Mohler *et al*., The type I membrane protein EFF-1 is essential for developmental cell fusion. *Dev. Cell* **2**, 355–362 (2002).
45. B. Podbilewicz, "Cell fusion" in *WormBook*, J. M. Kramer, D. G. Moerman, eds. (The C. elegans Research Community, WormBook, 2006).
46. M. Oren-Suissa, D. H. Hall, M. Treinin, G. Shemer, B. Podbilewicz, The fusogen EFF-1 controls sculpting of mechanosensory dendrites. *Science* **328**, 1285–1288 (2010).
47. T. Zhu, X. Liang, X. M. Wang, K. Shen, Dynein and EFF-1 control dendrite morphology by regulating the localization pattern of SAX-7 in epidermal cells. *J. Cell Sci.* **130**, 4063–4071 (2017).
48. B. Neumann *et al*., EFF-1-mediated regenerative axonal fusion requires components of the apoptotic pathway. *Nature* **517**, 219–222 (2015).
49. A. Ghosh-Roy, Z. Wu, A. Goncharov, Y. Jin, A. D. Chisholm, Calcium and cyclic AMP promote axonal regeneration in *Caenorhabditis elegans* and require DLK-1 kinase. *J. Neurosci.* **30**, 3175–3183 (2010).
50. D. M. Rosenbaum, S. G. Rasmussen, B. K. Kobilka, The structure and function of G-protein-coupled receptors. *Nature* **459**, 356–363 (2009).
51. D. Calebiro, T. Sungkaworn, Single-molecule imaging of GPCR interactions. *Trends Pharmacol. Sci.* **39**, 109–122 (2018).
52. T. Sungkaworn *et al*., Single-molecule imaging reveals receptor-G protein interactions at cell surface hot spots. *Nature* **550**, 543–547 (2017).
53. F. Persson, M. Lindén, C. Unoson, J. Elf, Extracting intracellular diffusive states and transition rates from single-molecule tracking data. *Nat. Methods* **10**, 265–269 (2013).
54. P. Padmanabhan, R. Martínez-Mármol, D. Xia, J. Götz, F. A. Meunier, Frontotemporal dementia mutant Tau promotes aberrant Fyn nanoclustering in hippocampal dendritic spines. *eLife* **8**, e45040 (2019).
55. M. Yanagawa *et al*., Single-molecule diffusion-based estimation of ligand effects on G protein-coupled receptors. *Sci. Signal.* **11**, eaao1917 (2018).
56. J. Zhang, S. S. Ferguson, L. S. Barak, L. Ménard, M. G. Caron, Dynamin and beta-arrestin reveal distinct mechanisms for G protein-coupled receptor internalization. *J. Biol. Chem.* **271**, 18302–18305 (1996).
57. C. B. Harper *et al*., Dynamin inhibition blocks botulinum neurotoxin type A endocytosis in neurons and delays botulism. *J. Biol. Chem.* **286**, 35966–35976 (2011).
58. C. B. Harper *et al*., Botulinum neurotoxin type-A enters a non-recycling pool of synaptic vesicles. *Sci. Rep.* **6**, 19654 (2016).
59. A. McCluskey *et al*., Building a better dynasore: The dyngo compounds potently inhibit dynamin and endocytosis. *Traffic* **14**, 1272–1289 (2013).
60. R. Nygaard *et al*., The dynamic process of β(2)-adrenergic receptor activation. *Cell* **152**, 532–542 (2013).
61. T. Uchański, E. Pardon, J. Steyaert, Nanobodies to study protein conformational states. *Curr. Opin. Struct. Biol.* **60**, 117–123 (2020).
62. D. P. Staus *et al*., Regulation of β2-adrenergic receptor function by conformationally selective single-domain intrabodies. *Mol. Pharmacol.* **85**, 472–481 (2014).
63. A. I. Öberg, N. Dehvari, T. Bengtsson, β-Adrenergic inhibition of contractility in L6 skeletal muscle cells. *PLoS One* **6**, e22304 (2011).
64. C. A. Moore, S. K. Milano, J. L. Benovic, Regulation of receptor trafficking by GRKs and arrestins. *Annu. Rev. Physiol.* **69**, 451–482 (2007).
65. A. R. B. Thomsen *et al*., GPCR-G protein-β-arrestin super-complex mediates sustained G protein signaling. *Cell* **166**, 907–919 (2016).
66. K. Jaqaman *et al*., Cytoskeletal control of CD36 diffusion promotes its receptor and signaling function. *Cell* **146**, 593–606 (2011).
67. F. Levet *et al*., SR-Tesseler: A method to segment and quantify localization-based super-resolution microscopy data. *Nat. Methods* **12**, 1065–1071 (2015).
68. W. K. Cho *et al*., RNA polymerase II cluster dynamics predict mRNA output in living cells. *eLife* **5**, e13617 (2016).
69. I. I. Cisse *et al*., Real-time dynamics of RNA polymerase II clustering in live human cells. *Science* **341**, 664–667 (2013).
70. G. G. Gross *et al*., Recombinant probes for visualizing endogenous synaptic proteins in living neurons. *Neuron* **78**, 971–985 (2013).
71. D. Choquet, A. Triller, The dynamic synapse. *Neuron* **80**, 691–703 (2013).
72. A. Kusumi, T. A. Tsunoyama, K. M. Hirosawa, R. S. Kasai, T. K. Fujiwara, Tracking single molecules at work in living cells. *Nat. Chem. Biol.* **10**, 524–532 (2014).
73. A. Echarri, M. A. Del Pozo, Caveolae—Mechanosensitive membrane invaginations linked to actin filaments. *J. Cell Sci.* **128**, 2747–2758 (2015).
74. R. G. Parton, M. A. del Pozo, Caveolae as plasma membrane sensors, protectors and organizers. *Nat. Rev. Mol. Cell Biol.* **14**, 98–112 (2013).
75. T. Hirama *et al*., Phosphatidylserine dictates the assembly and dynamics of caveolae in the plasma membrane. *J. Biol. Chem.* **292**, 14292–14307 (2017).
76. E. Boucrot, M. T. Howes, T. Kirchhausen, R. G. Parton, Redistribution of caveolae during mitosis. *J. Cell Sci.* **124**, 1965–1972 (2011).
77. K. Smurova, B. Podbilewicz, RAB-5- and DYNAMIN-1-mediated endocytosis of EFF-1 fusogen controls cell-cell fusion. *Cell Rep.* **14**, 1517–1527 (2016).
78. A. Manglik *et al*., Structural insights into the dynamic process of β2-adrenergic receptor signaling. *Cell* **161**, 1101–1111 (2015).
79. X. J. Yao *et al*., The effect of ligand efficacy on the formation and stability of a GPCR-G protein complex. *Proc. Natl. Acad. Sci. U.S.A.* **106**, 9501–9506 (2009).
80. M. Scarselli, P. Annibale, A. Radenovic, Cell type-specific β2-adrenergic receptor clusters identified using photoactivated localization microscopy are not lipid raft related, but depend on actin cytoskeleton integrity. *J. Biol. Chem.* **287**, 16768–16780 (2012).
81. S. Ganguly, R. Saxena, A. Chattopadhyay, Reorganization of the actin cytoskeleton upon G-protein coupled receptor signaling. *Biochim. Biophys. Acta* **1808**, 1921–1929 (2011).
82. C. B. Harper, M. R. Popoff, A. McCluskey, P. J. Robinson, F. A. Meunier, Targeting membrane trafficking in infection prophylaxis: Dynamin inhibitors. *Trends Cell Biol.* **23**, 90–101 (2013).
83. A. Gulyani *et al*., A biosensor generated via high-throughput screening quantifies cell edge Src dynamics. *Nat. Chem. Biol.* **7**, 437–444 (2011).
84. T. Kükenshöner *et al*., Selective targeting of SH2 domain-phosphotyrosine interactions of Src family tyrosine kinases with monobodies. *J. Mol. Biol.* **429**, 1364–1380 (2017).
85. R. H. Newman, M. D. Fosbrink, J. Zhang, Genetically encodable fluorescent biosensors for tracking signaling dynamics in living cells. *Chem. Rev.* **111**, 3614–3666 (2011).
86. R. Tamaskovic *et al*., Intermolecular biparatopic trapping of ErbB2 prevents compensatory activation of PI3K/AKT via RAS-p110 crosstalk. *Nat. Commun.* **7**, 11672 (2016).
87. A. Keppler, H. Pick, C. Arrivoli, H. Vogel, K. Johnsson, Labeling of fusion proteins with synthetic fluorophores in live cells. *Proc. Natl. Acad. Sci. U.S.A.* **101**, 9955–9959 (2004).
88. G. V. Los *et al*., HaloTag: A novel protein labeling technology for cell imaging and protein analysis. *ACS Chem. Biol.* **3**, 373–382 (2008).
89. H. Liu *et al*., Visualizing long-term single-molecule dynamics in vivo by stochastic protein labeling. *Proc. Natl. Acad. Sci. U.S.A.* **115**, 343–348 (2018).
90. M. Kirkham *et al*., Evolutionary analysis and molecular dissection of caveola biogenesis. *J. Cell Sci.* **121**, 2075–2086 (2008).
91. S. Brenner, The genetics of *Caenorhabditis elegans*. *Genetics* **77**, 71–94 (1974).
92. J. Giacomotto, S. Rinkwitz, T. S. Becker, Effective heritable gene knockdown in zebrafish using synthetic microRNAs. *Nat. Commun.* **6**, 7378 (2015).